Airborne DInSAR Results Using Time-Domain Backprojection Algorithm: A Case Study Over the Slumgullion Landslide in Colorado With Validation Using Spaceborne SAR, Airborne LiDAR, and Ground-Based Observations

Ning Cao, Hyongki Lee, Evan Zaugg, Ramesh Shrestha, William Carter, Craig Glennie, Guoquan Wang, Zhong Lu, and Juan Carlos Fernandez-Diaz

***Abstract*—The major impediment to accurate airborne repeat-pass differential synthetic aperture radar (SAR) interferometry (DInSAR) is compensating for aircraft motion caused by air turbulence. Various motion compensation (MoCo) procedures have been used in the airborne DInSAR processing to acquire reliable deformation mapping. In this paper, we present the use of time-domain backprojection (BP) algorithm for SAR focusing in an airborne DInSAR survey: No MoCo procedure is needed because the BP algorithm is inherently able to compensate for platform motion. In this study, we present the results of a pilot study aimed at demonstrating the feasibility of deformation mapping with an airborne SAR system based on the monitoring of the Slumgullion landslide in Colorado, USA between July 3 and 10 of 2015. The employed airborne SAR system is an Artemis SlimSAR that is a compact, modular, and multi-frequency radar system. Airborne light detection and ranging and global navigation satellite system (GNSS) observations, as well as spaceborne DInSAR results using COSMO-SkyMed (CSK) images, were used to verify the performance of the airborne SAR system. The surface velocities of the landslide derived from the airborne DInSAR observations showed good agreement with the GNSS and spaceborne DInSAR estimates. A three-dimensional deformation map of the Slumgullion landslide was also generated, which displayed distinct correlation between the landslide motion and topographic variation. This study shows that an inexpensive airborne *L*-band DInSAR system has the potential to measure centimeter level deformation with flexible temporal and spatial baselines.**

Manuscript received March 3, 2017; revised June 28, 2017; accepted August 3, 2017. Date of publication August 22, 2017; date of current version November 7, 2017. This work was supported by the National Center for Airborne Laser Mapping via project NSF EAR-1043051. *(Corresponding author: Hyongki Lee.)*

N. Cao, H. Lee, R. Shrestha, W. Carter, C. Glennie, and J. C. Fernandez-Diaz are with the Department of Civil and Environmental Engineering and the National Center for Airborne Laser Mapping, University of Houston, Houston, TX 77204 USA (e-mail: ncao5@uh.edu; hlee@uh.edu; rshrest2@Central.UH.EDU; carter4451@bellsouth.net; clglennie@uh.edu; jfernan4@Central.UH.EDU).

E. Zaugg is with the Artemis, Inc., Hauppauge, NY 11788 USA (e-mail: evan@artemisinc.net).

G. Wang is with the Department of Earth and Atmospheric Sciences, University of Houston, Houston, TX 77004 USA (e-mail: gwang@uh.edu).

Z. Lu is with the Roy M. Huffington Department of Earth Sciences, Southern Methodist University, Dallas, TX 75205 USA (e-mail: zhonglu@mail.smu.edu).

Color versions of one or more of the figures in this paper are available online at http://ieeexplore.ieee.org.

Digital Object Identifier 10.1109/JSTARS.2017.2737362

***Index Terms*—Backprojection (BP), differential synthetic aperture radar interferometry (DInSAR), InSAR, landslide, motion compensation (MoCo), residual motion error (RME), SAR.**

I. Introduction

DIFFERENTIAL Synthetic aperture radar (SAR) interferometry (DInSAR) is a technique that uses two or more SAR images to estimate ground surface displacement at the millimeter or centimeter accuracy level, depending on the radar frequency and interferogram coherence. A major drawback of the traditional DInSAR technique is that only deformation along the line-of-sight (LOS) can be obtained. Because spaceborne SAR systems fly along near-polar, sun-synchronous orbits, they are limited to observe accurate deformation occurring close to the North–South direction (except in polar regions). Even though spaceborne DInSAR can now retrieve three-dimensional (3-D) deformations by exploiting both the right- and left-looking capability [e.g., ALOS PALSAR-2, and COSMO-SkyMed (CSK)], the accuracy of the estimated North–South deformation still tends to be much worse than the East–West or vertical components according to [1] where it was reported that the standard errors of observed deformation were 0.8, 3.4, and 0.7 cm in East–West, North–South, and Vertical directions, respectively. Compared with spaceborne SAR, airborne SAR systems have the advantages of flexible scanning geometry and revisit times, and higher spatial resolution. Therefore, it is expected that the routine use of airborne DInSAR could greatly expand access to the observational data for researchers to better characterize, quantify, and understand the behavior of many natural hazards [2]. However, only a few airborne SAR systems have been successfully deployed for deformation mapping through repeat-pass interferometry, such as the E-SAR (and its successor F-SAR) system from the German Aerospace center (DLR) [3], UAVSAR from the Jet Propulsion Laboratory [4], and OrbiSAR from OrbiSat [5].

Unlike spaceborne SAR that has fairly stable trajectories, the major challenge for processing airborne SAR data is

compensating the trajectory deviations. In recent years, various motion compensation (MoCo) procedures have been proposed [6]–[14]. In order to compensate for motion errors trajectory information must be acquired, generally by a combination of global navigation satellite system (GNSS) and Inertial Measurement Unit (IMU) systems. Recent improvements in the GNSS/IMU navigation technology enabled the determination of aircraft trajectories with an estimated precision of a few centimeters [15], [16]. The basic procedure of MoCo is: 1) generating a linear reference trajectory that best-fits the actual trajectory, and 2) calculating and applying motion corrections. It is also necessary to use an external digital elevation model (DEM) in the MoCo procedure to make range-dependent phase corrections [8]–[11]. A center-beam (CB) approximation is also commonly used to improve computational efficiency at the expense of degrading the phase accuracy [5], [18].

Even after applying MoCo, errors in the trajectory estimated from the GNSS/IMU system, referred to as residual motion error (RME), still exist and can cause erroneous phase undulations in the final interferogram. Several efforts have attempted to estimate and remove the RME [12]–[17]. For example, in [12]–[16], multisquint techniques were used to estimate the RME from the registration error. Through an aperture splitting procedure, SAR images with different squint angles can be obtained, and the corresponding interferograms can be generated. Then the residual baseline errors can be estimated from the phase differences between the interferograms. In addition to the multisquint method, advanced autofocus algorithms have been proposed to compensate RME [17]. In this study, the multisquint method is used for the RME correction.

In addition to the MoCo methods mentioned above, the time-domain backprojection (BP) technique can also focus the SAR data obtained from nonlinear platform trajectories [19]–[24]. Unlike the frequency-domain SAR image formation techniques, the time-domain BP method requires trajectory data as well as a reconstruction-grid (such as a DEM) to be known [23], [24]. Compared with frequency-domain focusing, the time-domain BP method has the advantages of:

1) focusing the data obtained from significantly nonlinear trajectories, which is common for airborne platforms (MoCo is inherently taken into account without the CB approximation). For wide-beam airborne SAR with large squint angle, MoCo becomes very complicated, in which case BP can be considered as an alternative to perform SAR focusing;
2) focusing the data directly on the desired reconstruction grid, thus, avoiding the need for geocoding;
3) applicable to data obtained from different acquisition modes such as the stripmap, terrain observation by progressive scans or ScanSAR modes.

The major drawback of the BP algorithm is its heavy computational burden, which can be mitigated by employing the fast-factorized BP method [22].

In this study, we present the airborne DInSAR results using the BP technique. In July 2015, a series of SAR collections, using the SlimSAR system developed by Artemis Inc., were made over the Slumgullion landslide in Colorado, USA. The Slumgullion landslide, located in the San Juan Mountains near Lake City, Colorado, is a long-term perpetual moving landslide with a continual downhill slide. Fig. 1 shows an optical image of the landslide area. The active portion of the landslide is 3.9 km long and has an average width of 300 m [25]. It is estimated that the active part of the landslide has been moving for about 300 years [26] and contains many individual kinematic elements with steady average annual speeds between 0.5 to 7 m/year [27]–[30]. It is also known that the landslide speed is related to subsurface water levels and sensitive to seasonal rainfalls; the speed of the landslide movement is highest during the spring snowmelt and significant rainfall events [31]. The Slumgullion landslide has been utilized in several ground-based, airborne, and spaceborne DInSAR studies due to the convenience of having such a large area of consistent motion [30], [32]–[37].

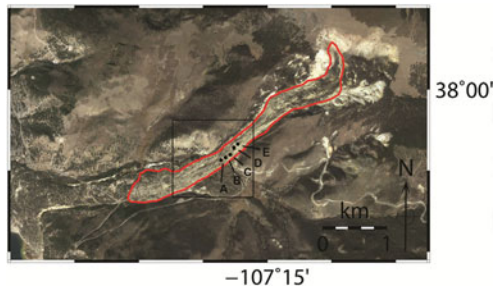

Fig. 1. Optical image of the Slumgullion landslide area from Google Earth with the red outline indicating the boundary of the active part and black dots indicating locations of the five GNSS stations used for validation in this study. The black rectangle denotes the coverage area for Figs. 9–12.

In addition to the airborne DInSAR measurements, spaceborne DInSAR, airborne light detection and ranging (LiDAR), and GNSS surveys were also performed simultaneously. The airborne LiDAR campaign provided high-resolution and high-accuracy topographic data over the study area, and differential GNSS surveys provided independent measurements of the landslide motion. An intercomparison between the deformation maps derived from airborne DInSAR and spaceborne DInSAR observations, which have different sources of errors, was also been performed.

This paper is organized as follows. A detailed description of the datasets used in this study including airborne SAR, spaceborne SAR, GNSS, and airborne LiDAR data is given in Section II. Section III provides an analysis of the BP algorithm as well as details regarding airborne and spaceborne DInSAR data processing strategies. Section IV is a description of the deformation maps generated from both airborne and spaceborne DInSAR. Section V outlines the analysis and discussion of DInSAR- and GNSS-derived landslide velocities. GNSS results were used to verify the DInSAR results in LOS directions. Then airborne and spaceborne DInSAR results were combined to generate 3-D deformation estimates, which were further compared to the 3-D GNSS estimates. Finally, the land motion from airborne DInSAR was also compared with that from spaceborne DInSAR. We conclude with Section VI that summarizes our findings.

TABLE I
PARAMETERS OF THE E-SAR, UAVSAR, ORBISAR, AND SLIMSAR SYSTEMS

	E-SAR	UAVSAR	OrbiSAR	SlimSAR
Center frequency (GHz)	1.325	1.2175–1.2975	9.55	1.3075
Bandwidth (MHz)	150	80	150	185
Pulse repeat frequency (Hz)	10000	350–855	1600	1510
Look angle range (deg)	25–65	25–65	NA	25–60
Altitude (above ground level) (m)	Up to 6000	2000–18000	8000	300–3000
Ground speed (m/s)	NA	100–250	108	34
Range swath (km)	12.5	22	4	2.5–8.5
Polarization	Quad-pol	Quad-pol	HH	Quad-pol
Peak transmit power (kW)	0.9	3.1	2.5	0.06
Range resolution (m)	1.5	1.67	1	1
Azimuth resolution (m)	0.4	0.8	1.2	1
Noise equivalent sigma0 (dB)	NA	<-50	NA	<-30
Antenna gain (dB)	NA	NA	NA	6
Receiver noise figure (dB)	NA	NA	NA	3
Weight (kg)	NA	210	NA	15
Antenna size (m)	NA	0.5×1.6	NA	0.15×0.15

Note: NA indicates the unknown parameters. Parameters of *L*-band E-SAR, *L*-band UAVSAR, *X*-band OrbiSAR, and *L*-band SlimSAR are given in the table. All the four SAR systems can also work in other frequency bands as shown in [2], [5], [15], [38]–[41].

Fig. 2. Installation of the *L*-band antennas (at the very top and bottom) on the wing strut.

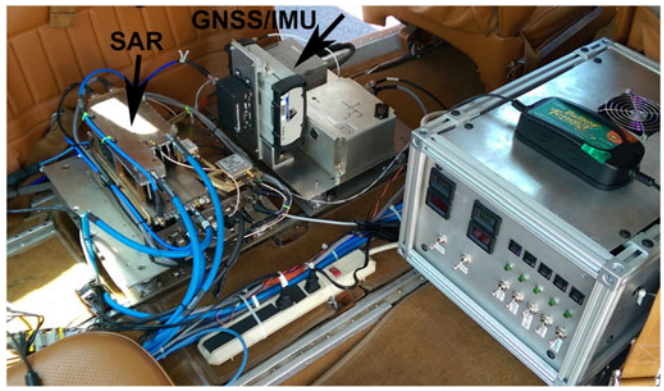

Fig. 3. SlimSAR SAR system with GNSS/IMU unit.

II. DATASET USED AND ACQUISITIONS STRATEGY

A. SlimSAR System and Data Acquisition Strategy

The airborne SAR system used in this study is an *L*-band system called SlimSAR developed by Artemis, Inc., based in Hauppauge, NY, USA. [2]. The SlimSAR system is a compact, multicapability radar system available in many different configurations. For this study, the SlimSAR was installed on a Cessna 206 aircraft. Details about the SlimSAR system along with E-SAR, UAVSAR, and OrbiSAR are summarized in Table I [2], [5], [15], [38]–[41]. Compared with other systems, the advantage of SlimSAR is its small size and low signal power, which makes it suitable for operation on small aircrafts and unmanned aerial vehicles.

The SlimSAR system was configured with two *L*-band antennas (Ch0 and Ch1) installed along the right wing strut of the airplane as shown in Fig. 2. The SlimSAR system can collect data from the two channels simultaneously. The *L*-band antennas, each used for both transmitting and receiving signals, provide two channels of radar data with VV polarization. The baseline between the two *L*-band antennas was 1.822 m [32]. The two channel radar data allowed us to implement both dual-antenna single-pass interferometry and single-antenna repeat-pass interferometry. The dual-antenna single-pass interferometry enabled us to generate a DEM [45]–[47], which is compared with other DEMs in Section III-B.

One important procedure of airborne SAR imaging is the acquisition of precise antenna position and its motion. The trajectory of the aircraft is measured using a GNSS/IMU system, which provides both real-time position and attitude information to the radar, and also stores the raw observations for posting processing (see Fig. 3). The post-processing enables more precise computation of aircraft trajectory by blending the airborne GNSS/IMU observations with ground GNSS observations collected simultaneously. The typical position accuracies of post-processed results are around 1 and 2 cm in horizontal and vertical directions, respectively [48], [49].

Airborne SAR flights were performed on July 3, 7, and 10 of 2015; during each flight multiple airborne SAR flight paths were made as shown in Fig. 4 [32]. Four flight paths (flight A, C, D, and E) were flown across the earthflow, each focusing on different portions of the slide. Moreover, we had another flight

TABLE II
FIVE AIRBORNE SAR FLIGHT PATHS USED IN THIS STUDY

Path	Heading angle	Look angle
A	317°	24°–65°
B	261°	31°–68°
C	317°	20°–66°
D	335°	44°–70°
E	354°	44°–66°

path (path B) was flown along the earthflow that covered the entire area in single image. The flight altitude is around 1066 m above ground level. The heading and look angles for these five paths are given in Table II.

B. Spaceborne DInSAR Data

Four *X*-band CSK spotlight images with 1-day interval were used to estimate the landslide deformation over the study area. The four images were acquired between July 24 and 26 of 2015 from both ascending and descending orbits as shown in Table III. The CSK constellation is an *X*-band SAR system with 3.1-cm wavelength and can be operated in different scanning modes that include spotlight, stripmap, and ScanSAR [50]. Because the average width of the landslide is only around 300 m, the high-resolution (1 m $\times$ 1 m) spotlight mode data were used. Moreover, the "tandem-like" interferometry configuration (i.e., 1-day interval between Master and Slave scannings) was used to minimize temporal decorrelation due to the fast landslide movement [52].

C. GNSS Measurements

To obtain deformation reference and validation data, five geodetic grade GNSS stations were installed along the center portion of the landslide as shown in Fig. 1. An additional reference station was also installed on a permanent monument outside the landslide. The baseline lengths for the five GNSS stations in relation to the reference station varied from 74 to 578 m. The observation duration at each GNSS site was between 5 and 7 h. The 3-D coordinates at each GNSS site were derived from these baselines, and displacements were estimated from temporally separated observations. The time window for two adjacent surveys was 7 days for site A and 3 days for the other four sites. TopconTools software package was employed to calculate the baselines and station coordinates using fixed ambiguity carrier-phase double difference observables [43], [44]. According to the previous investigations, the differential processing with baselines shorter than 1 km and occupation periods longer than 4 h can achieve horizontal accuracy of 2 to 3 mm and vertical accuracy of 4 to 6 mm [43], [44]. The estimated deformation rates at these five GNSS stations between July 3 and July 10 of 2015 are summarized in Table IV. The GNSS results indicate that the observed segment of the landslide experienced fairly coherent movement during the survey period. The horizontal velocity was about 1.3 to 1.5 cm/day toward the southwest. As will be discussed in Section V, the GNSS results were used as the ground truth to verify the DInSAR-derived landslide movements from the airborne and spaceborne platforms.

D. Airborne LiDAR Data

The airborne LiDAR campaign was conducted by the National Center for Airborne Laser Mapping (NCALM) using an Optech Gemini NIR LiDAR system installed on a Piper Chieftain PA-31 aircraft. The Gemini system can provide up to four discrete returns for each laser pulse and both vegetation and the "bare earth" information can be extracted from the discrete return data. Therefore, two types of LiDAR surface models were obtained: an unfiltered or first return digital surface model (LiDAR DSM), and a bare-earth DEM (LiDAR DEM). Airborne LiDAR provided an accurate ($<$10 cm vertical error with 0.5 m spatial resolution) topographic model of the landslide area. Fig. 5 shows the LiDAR hillshade DEM overlaid on a Google Earth optical image. The LiDAR DEM was used in the analysis of DEM error estimation in Section III-B and spaceborne DInSAR processing using the X-band CSK data in Section III-C.

III. DATA PROCESSING STRATEGY

A. Signal Analysis of the BP Technique

A brief derivation of the time-domain BP algorithm for a point target is given in this section. The transmitted signal of the radar is normally a "chirp" (linear frequency modulated signal). For simplicity, the following analysis is based on stop–go approximation, i.e., the antenna remains at the same location during the transmitting and receiving of one pulse. Under the stop–go approximation, the SAR focusing can be broken into two separate steps (range and azimuth compressions). The effect of the stop–go approximation on the focused SAR image is beyond the scope of this paper. After demodulation and range-compression, the range-compressed signal can be given by

$$s_{\mathrm{RC}}(i) = A_i \exp\{-j2\pi f_0 \tau_i\} \tag{1}$$

where i is the slow-time pulse index, A_i is the amplitude, f_0 is the center frequency, τ_i is the two-way propagation time from the radar antenna to the target. Assuming R_i is the real range from the radar to the phase center of the target, we have $\tau_i = 2R_i/c$. An important step for the BP algorithm is to compensate the phase component in (1) using the estimated two-way propagation time $\tilde{\tau}_i$. Here $\tilde{\tau}_i$ can be estimated from $\tilde{\tau}_i = 2\tilde{R}_i/c$, where $\tilde{R}_i$ is the estimated radar-target range from the radar position to the physical center of a scattering cell. In general, the target is assumed to be located at the center of the pixel. Therefore, as shown in Fig. 6, $\tilde{R}_i$ can be estimated from the SAR scanning geometry using the trajectory information and specified reconstruction grid. Then we obtain the phase-compensated signal $s_{\mathrm{RC}}^{\mathrm{comp}}(i)$ as

$$\begin{aligned} s_{\mathrm{RC}}^{\mathrm{comp}}(i) &= s_{\mathrm{RC}}(i) \exp\{j2\pi f_0 \tilde{\tau}_i\} \\ &= A_i \exp\left\{-j2\pi f_0 (2R_i/c - 2\tilde{R}_i/c)\right\} \\ &= A_i \exp\{-jk\Delta R_i\} \end{aligned} \tag{2}$$

TABLE III
FOUR CSK SPOTLIGHT IMAGES USED IN THIS STUDY

Dates		Perpendicular baselines (m)	Heading angle	Incidence angle
Master	Slave			
20150724	20150725	−752	352° ascending	53°
20150725	20150726	911	189° descending	47°

TABLE IV
DEFORMATION ESTIMATES FROM THE FIVE GNSS STATIONS ALONG THE LANDSLIDE AREA

GNSS station	Latitude (degree)	Longitude (degree)	Velocity (cm/day) North	East	Vertical
A	37°59'28.62404"	−107°15'25.75512"	−0.80	−1.10	−0.30
B	37°59'29.78718"	−107°15'23.22303"	−0.87	−0.93	−0.10
C	37°59'31.08267"	−107°15'20.56011"	−0.87	−0.97	−0.13
D	37°59'33.99763"	−107°15'18.58613"	−0.93	−0.97	−0.30
E	37°59'35.51689"	−107°15'16.33610"	−0.97	−1.17	−0.10

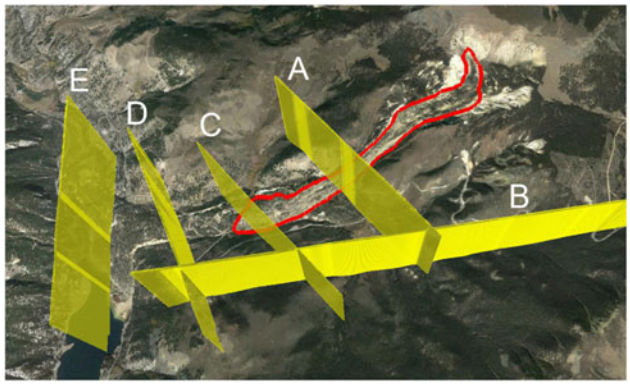

Fig. 4. 3-D view of the five airborne flight paths over the Slumgullion landslide area.

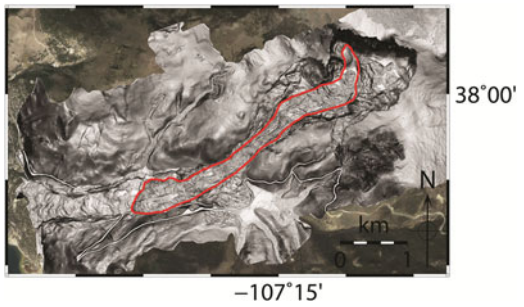

Fig. 5. Airborne LiDAR hillshade DEM overlaid on Google Earth optical image.

where $k = 4\pi/\lambda$ and $\Delta R_i = R_i - \tilde{R}_i$. λ is the wavelength. For simplification, here we assume that precise trajectory data are available for radar position. In practice, the residual trajectory error can also be estimated using the multisquint or autofocus methods [12]–[17]. It should be noted that range migration correction procedure is not needed in the BP algorithm because the range values can be directly estimated from the trajectory data and reconstruction grid.

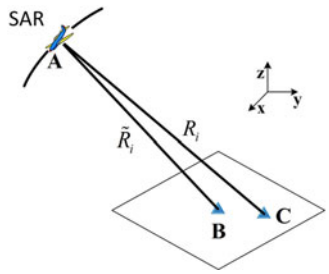

Fig. 6. SAR scanning geometry of one pixel. Point A, B, and C are the position of the SAR antenna, physical center, and actual phase center of a scattering target, respectively.

A basic BP process is to coherently integrate the phase-compensated range-compressed radar echoes $s_{\mathrm{RC}}^{\mathrm{comp}}(i)$ to form the image. For a point target, the backprojected signal is

$$I_{\mathrm{BP}} = \sum_{i=-N}^{M} s_{\mathrm{RC}}^{\mathrm{comp}}(i) = \sum_{i=-N}^{M} A_i \exp\{-jk\Delta R_i\}. \quad (3)$$

Here i is assumed to vary from $-N$ to M during the integration along the azimuth. For a system with zero squint angle, we have $N = M$. The range difference ΔR_i comes from the offset between the physical center and phase center of a scattering cell. Therefore, we can see that the backprojected signal I_{BP} contains the "residual phase" caused by range difference ΔR_i [24]. In order to further study the properties of the BP algorithm, a detailed analysis of this "residual phase" is needed.

In Fig. 6, point A, B, and C represent the position of the SAR antenna, physical center, and actual phase center of a scattering target, respectively. For further analysis, the coordinates of point A, B, and C in Fig. 6 are set to (x_A, y_A, z_A), (x_B, y_B, z_B), and (x_C, y_C, z_C), respectively. Assuming the offset vector between point B and C is $\boldsymbol{\varepsilon}(\varepsilon_x, \varepsilon_y, \varepsilon_z) = \mathbf{C}–\mathbf{B}$, range R_i and $\tilde{R}_i$ can be

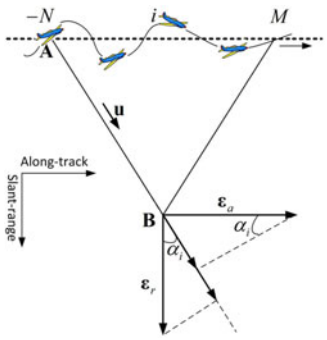

Fig. 7. Decomposition of the offset vector $\boldsymbol{\varepsilon}'$ into slant-range and along-track directions.

expressed as [24]

$$\begin{aligned}\tilde{R}_i &= \|\mathbf{A}-\mathbf{B}\| \\ &= \sqrt{(x_A-x_B)^2+(y_A-y_B)^2+(z_A-z_B)^2} \\ R_i &= \|\mathbf{A}-\mathbf{C}\| = \|\mathbf{A}-\mathbf{B}-\boldsymbol{\varepsilon}\| \\ &\approx \tilde{R}_i - \frac{(\mathbf{A}-\mathbf{B})\times\boldsymbol{\varepsilon}}{\|\mathbf{A}-\mathbf{B}\|}. \end{aligned} \tag{4}$$

Therefore, the range difference ΔR_i can be estimated from (4) as

$$\Delta R_i = R_i - \tilde{R}_i \approx \frac{(\mathbf{B}-\mathbf{A})\cdot\boldsymbol{\varepsilon}}{\|\mathbf{B}-\mathbf{A}\|} = \boldsymbol{\mu}\cdot\boldsymbol{\varepsilon} \tag{5}$$

where $\boldsymbol{\mu} = \frac{\mathbf{B}-\mathbf{A}}{\|\mathbf{B}-\mathbf{A}\|}$ is the unitary vector from Point A to B. Therefore, we can see that the range difference ΔR_i can be estimated by the length of the component of vector $\boldsymbol{\varepsilon}$ in the instantaneous $\mathbf{AB}$ direction during the scanning. The approximation in (5) is valid since vector $\mathbf{AB}$ and vector $\mathbf{AC}$ can be assumed to be parallel. Since vector $\boldsymbol{\varepsilon}$ is not on the slant-range and along-track plane like vector $\mathbf{AB}$, only the partial component of vector $\boldsymbol{\varepsilon}$ in this plane can make a contribution to the range difference in (5). Therefore, we assume the component of vector $\boldsymbol{\varepsilon}$ on the slant-range and along-track plane is $\boldsymbol{\varepsilon}'$.

For further analysis, we decompose the offset vector $\boldsymbol{\varepsilon}'$ into the slant-range and along-track directions as $\boldsymbol{\varepsilon}' = \boldsymbol{\varepsilon}_r + \boldsymbol{\varepsilon}_a$. As shown in Fig. 7, ΔR_i can be obtained as

$$\begin{aligned}\Delta R_i &= \boldsymbol{\mu}\cdot\boldsymbol{\varepsilon} = \boldsymbol{\mu}\cdot\boldsymbol{\varepsilon}' = \boldsymbol{\varepsilon}_r\cdot\boldsymbol{\mu} + \boldsymbol{\varepsilon}_a\cdot\boldsymbol{\mu} \\ &= \|\boldsymbol{\varepsilon}_r\|\cos\alpha_i + \|\boldsymbol{\varepsilon}_a\|\sin\alpha_i \\ &= \varepsilon_r\cos\alpha_i + \varepsilon_a\sin\alpha_i \end{aligned} \tag{6}$$

where α_i is the angle between vector $\mathbf{AB}$ and the slant-range direction. It should be noted that the system squint angle is assumed to be zero and the slant-range direction here is the slant range direction at zero Doppler time. For the cases of nonzero Doppler centroid, a similar result can be obtained. During the scanning, vector $\mathbf{AB}$ can be regarded as the instantaneous LOS direction. Consequently, α_i can be regarded as the instantaneous squint angle. Substituting (6) into (2) we can obtain

$$\begin{aligned}s_{\mathrm{RC}}^{\mathrm{comp}}(i) &= A_i\exp\{-jk\varepsilon_r\cos\alpha_i - jk\varepsilon_a\sin\alpha_i\} \\ &\approx A_i\exp\{-jk\varepsilon_r - jk\varepsilon_a\alpha_i\}. \end{aligned} \tag{7}$$

Since α_i is very small ($<$ 2°– 5° for airborne SAR, and $< 3\times10^{-6}$° for spaceborne SAR), we have $\cos\alpha_i \approx 1$ and $\sin\alpha_i \approx \alpha_i$. Interestingly, the signal $s_{\mathrm{RC}}^{\mathrm{comp}}(i)$ has constant phase and linear phase components after this approximation.

For simplification, we assume that the system squint angle is zero and $M = N$. Therefore, (3) becomes

$$I_{\mathrm{BP}} \approx \sum_{i=-N}^{N} A_i\exp\{-jk\varepsilon_r - jk\varepsilon_a\alpha_i\}. \tag{8}$$

Assuming the response of the target is symmetric with respect to $i = 0$, which means $A_i \approx A_{-i}$ and $\alpha_i = -\alpha_{-i}$, (8) can be rewritten as

$$\begin{aligned}I_{\mathrm{BP}} &= A_0\exp\{-jk\varepsilon_r\} + \sum_{i=1}^{N}(A_i\exp\{-jk\varepsilon_r\}\cdot 2\cos(k\varepsilon_a\alpha_i)) \\ &= A_0\exp\{-jk\varepsilon_r\} + \sum_{i=1}^{N}(A'_i\exp\{-jk\varepsilon_r\}) \end{aligned} \tag{9}$$

where $A'_i = 2A_i\cos(k\varepsilon_a\alpha_i)$. From (9), it can be seen that the essence of the BP algorithm is a coherent summation procedure. The BP algorithm also only contains the information of range offset ε_r. Therefore, the backprojected signal I_{BP} for a scattering cell has the form of

$$I_{\mathrm{BP}} \approx |I_{\mathrm{BP}}|\exp\{-jk\varepsilon_r\}. \tag{10}$$

For BP-focused single-look-complex (SLC) images, we can see that the known phase components caused by range $\tilde{R}_i$ have already been removed, leaving a residual phase caused by the unknown range offset ε_r from the physical center to the phase center of the scattering cell.

It is known that the azimuth-compressed signal for one target in the frequency domain has the following form:

$$I_{\mathrm{Freq}} \approx |I_{\mathrm{Freq}}|\exp\{-jkR_0\} \tag{11}$$

where R_0 is the shortest range from the antenna to the target at time $i = 0$, in which case $\Delta R_0 = R_0 - \tilde{R}_0 = \varepsilon_r$. Since $\tilde{R}_0$ is known from the geometry, we can add back the phase component of $\tilde{R}_0$ into I_{BP} as

$$\begin{aligned}I_{\mathrm{BP}}\exp\left\{-jk\tilde{R}_0\right\} &= |I_{\mathrm{BP}}|\exp\left\{-jk\left(\varepsilon_r+\tilde{R}_0\right)\right\} \\ &= |I_{\mathrm{BP}}|\exp\{-jkR_0\}. \end{aligned} \tag{12}$$

Comparing (12) with (11), it can be seen that the BP algorithm obtains the same phase component as frequency domain focusing methods. Therefore, we can perform the SAR interferometry in the slant-range direction using the backprojected signal I_{BP}. In practice, it is not necessary to add back the phase component of $\tilde{R}_0$ into I_{BP}. The differential interferogram can be directly obtained by calculating the complex conjugate multiplication of the backprojected signals I_{BP} of the master and

slave data. In other words, unlike frequency-domain differential interferometry, the time-domain slant-range interferometry can be implemented without the procedure of flattening and removing topographic phase components. For clarification, in this study, all the interferograms are the DInSAR images generated from signals I_{BP}. It should also be noted that the BP-focused images are inherently geo-registered and projected onto the reconstruction grid [20], [23]. Therefore, no geocoding is needed in the interferometry procedure.

In the BP method, the motion of the platform is compensated by calculating the range $\tilde{R}_i$ and removing the corresponding phase component. In other words, the MoCo is inherently applied to every individual target, and no CB approximation is needed. Therefore, the BP technique can fully compensate the aberrations caused by the trajectory turbulence. However, it should be noted that the antenna positions are assumed to be known precisely in the analysis above. Therefore, in practice, the RME can be introduced by an inaccurate trajectory estimated from the GNSS/IMU system, and the phase accuracy mainly depends on the accuracies of the trajectory measurements and DEM. How to remove the DEM error and RME will be discussed in the following section.

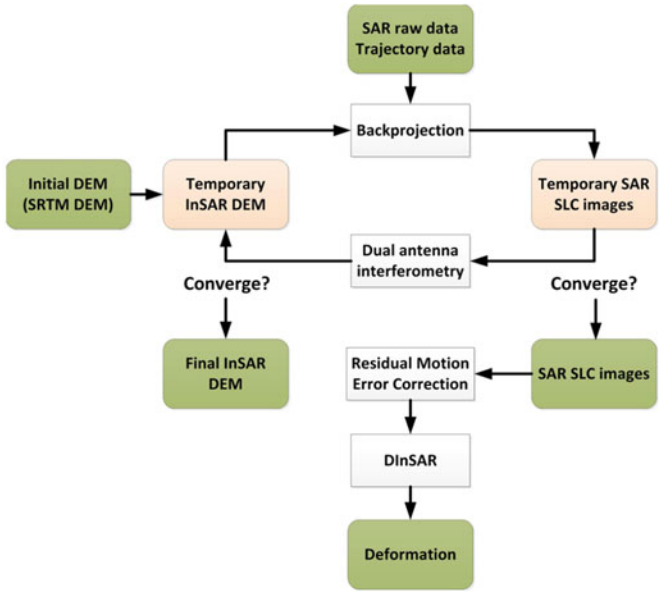

Fig. 8. Flowchart of the airborne DInSAR data processing.

B. Airborne SAR Data Processing

As mentioned in previous section, the DEM error and the RME of trajectory estimates can lead to amplitude and phase errors in the SAR image. The effects of DEM error on the BP-focused image and interferometric phase have been studied in [24], [53], [54]. It has been found that the interferometric phase varies slowly as the DEM error increases. It was suggested that an iteration procedure can be used to remove DEM errors [54]. In this study, we corrected the DEM error using the dual-antenna single-pass interferometry and the RME using the multisquint method described in [12], [13]. The flowchart of airborne SAR data processing is shown in Fig. 8. First of all, a DEM is generated from the dual-antenna single-pass interferometry through an iterative process [54]. For the dual-antenna single-pass interferometry, the RME tends to be similar for the two channels and tend to cancel out in the interferometry procedure [5]. Therefore, the differential interferogram generated from the dual-antenna single-pass interferometry is directly proportional to the magnitude of the DEM error, and the phase information can be used to correct the DEM. Specifically, the SAR images were first formed by the BP algorithm with an initial DEM, which may be of low quality or resolution; for example, the Shuttle Radar Topography Mission (SRTM) DEM with 30 m spatial resolution can be used. Then the DEM corrections were calculated from the dual-antenna single-pass interferogram, and the SAR data were reprocessed using the improved DEM. This process was iterated until the interferogram showed no DEM errors. Next the RME correction was implemented using the multisquint technique described in [12], [13]. First, we can create two SLC images with different squints using the master raw data by a split-aperture processing in azimuth. Then we interfere each of them with the corresponding looks using the slave raw data. Finally, the differential phases can be obtained by the complex conjugate multiplication of the two interferograms from the two subapertures. In short, the RME can be estimated by integrating the phase error difference between two subapertures as [13]

$$\phi_{\mathrm{err,res}}(x,r) = \int \frac{\phi_{\mathrm{diff}}(x',r)}{\Delta x(r)} dx' + \text{Constant} \qquad (13)$$

where x and r denote the azimuth and range positions, respectively, ϕ_{diff} is the differential phases of two interferograms generated from the two subapertures, Δx is the azimuth distance between the center of these two subapertures.

Multisquint technique can be used to estimate low frequency nonlinear RME. One key factor is the bandwidth of the subaperture. A long subaperture cancels out frequency components of RME higher than the subapertures' bandwidth [12]. In other words, multisquint technique only estimates the average of the true RME. The larger the subaperture, the less accurate the estimation of the high-frequency RME. However, if the subaperture is too short, the differential phases become noisy. As discussed in [14], the optimal bandwidth depends on the coherence and magnitude of RME and should be selected on a case-by-case basis. In this study, the bandwidth of the two subapertures was set to be 35 Hz each and with center frequencies of -17.5 and 17.5 Hz.

Moreover, the global constant and linear components of RME cannot be directly estimated in the integration procedure of the multisquint technique. One way to estimate the constant and linear RME is described in [14]: Fitting the differential interferogram with a model and estimating the unknown parameters using weighted least squares estimation. After removing RME, the ground deformation is estimated from DInSAR with single-antenna repeat-pass interferometry using either channel (Ch0 or Ch1).

As an example, an InSAR-derived (or InSAR-corrected) DEM segment (indicated by the black rectangle in Fig. 1) is

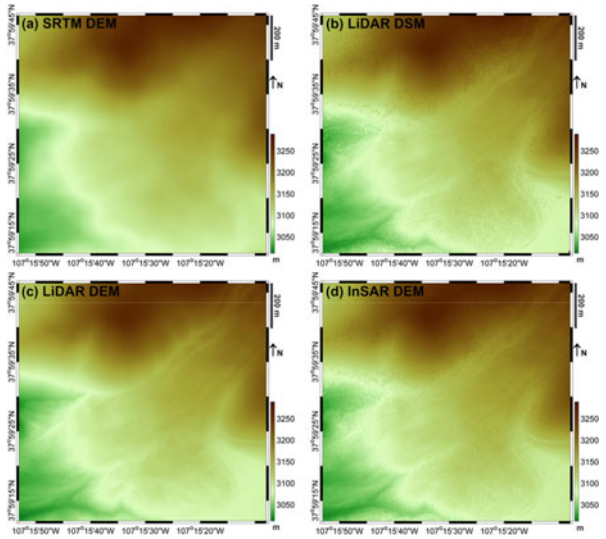

Fig. 9. Comparison of (a) SRTM DEM, (b) LiDAR DSM, (c) LiDAR DEM, and (d) airborne InSAR DEM.

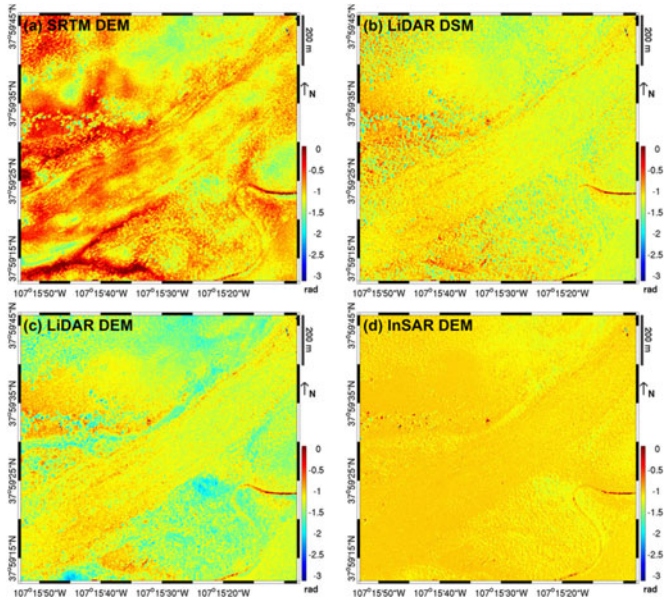

Fig. 10. Dual-antenna single-pass interferograms generated with different DEMs. (a)–(d) are generated using SRTM DEM, LiDAR DSM, LiDAR DEM, and InSAR DEM, respectively.

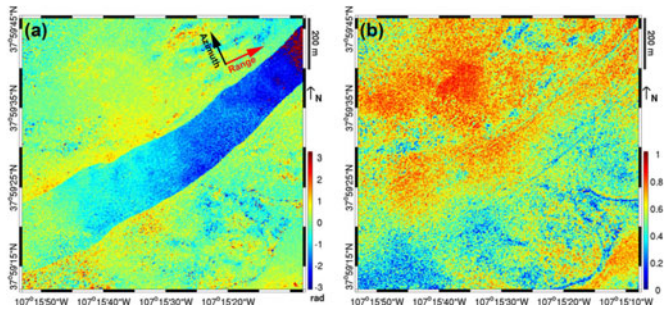

Fig. 11. (a) Repeat-pass wrapped interferogram and (b) coherence values of InSAR pair 07032015_105554-07072015_104040 without RME correction.

shown in Fig. 9 along with the SRTM DEM, LiDAR DSM, and LiDAR DEM. The InSAR DEM was generated from the iteration procedure as shown in Fig. 8 using the SRTM DEM as the initial DEM. It has been found that using the high resolution LiDAR DEM as the initial DEM gives similar results. It can also be seen from Fig. 9 that the InSAR-derived DEM and LiDAR DSM/DEM have much better resolutions ($\leq$1 m) and topographic details than the SRTM DEM (30-m resolution). Therefore, we can conclude that the DEM error has been corrected using the dual-antenna single-pass interferometry with an iterative procedure.

In order to further investigate whether the DEM error has been successfully removed, dual-antenna single-pass interferograms using initial SRTM, LiDAR, and InSAR DEMs were generated and presented in Fig. 10 using data acquired on 07032015_105554 (mmddyyyy_hhmmss). The dual-antenna single-pass interferograms were obtained by directly calculating the phase difference between two SAR images from Ch0 and Ch1. The SAR images were focused by the BP algorithm with using SRTM, LiDAR, and InSAR DEMs, respectively. It should be noted that the phase difference between these two channels should be a constant value if no DEM error exists, because the topographic phase components have been removed inherently in the BP focusing process. However, since channel Ch0 and channel Ch1 are not perfectly phase matched, the interferometric phase is not exactly zero even when there is no DEM errors. In this case, the interferometric phase has a nominal value of -1.16 when there is no DEM errors. In Fig. 10(a), we can see that significant residual phase errors exist when using the SRTM DEM, which indicates the existence of a significant DEM error. On the contrary, as can be seen in Fig. 10(d), the single-pass interferogram generated with the InSAR DEM shows negligible phase errors. Therefore, we can see that the error in the initial DEM used in the iteration process has been successfully removed. Interestingly, from Fig. 10(b) and (c), we can see some phase errors caused by the "errors" in LiDAR DSM/DEM, especially for the nonlandslide area covered by vegetation. The phase error in Fig. 10(b) and (c) is caused by the fact that laser and microwave radiation have different penetrating capabilities and their returns are produced by different backscattering centers. In other words, even though LiDAR DSM/DEM are more accurate, they do not "fit" the SAR data as the InSAR DEM represents the effective heights of the scatterers.

After removing the DEM errors using dual-antenna single-pass interferometry, SAR SLC images can then be obtained, and repeat-pass DInSAR can be implemented. First, a single-antenna repeat-pass interferogram without RME correction was computed as shown in Fig. 11. The temporal baseline is 4 days and the deviation between the two repeat tracks is within a 15-m tube. The movement of the landslide is clearly visible when compared to the nonmoving areas surrounding the slide. We observe the surface displacement due to the landslide gradually increase from the bottom to the top. The average coherence of the interferogram is 0.5. For this interferogram, RME was

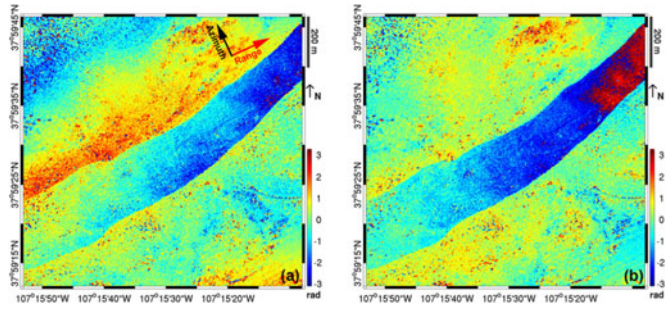

Fig. 12. Repeat-pass wrapped interferograms for InSAR pair 07032015_103909-07072015_104040 before (a) and after (b) RME correction.

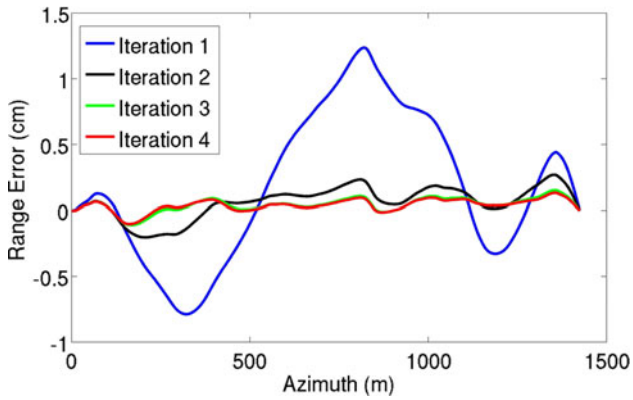

Fig. 13. Estimated residual baseline error in LOS direction of InSAR pair 07032015_103909-07072015_104040 (for middle range).

very small due to insignificant turbulence and, therefore, no RME correction was necessary.

In contrast, Fig. 12 shows a case where airborne DInSAR performance was noticeably improved by applying the RME correction. Fig. 12(a) shows that residual phase errors exist even after the DEM error was removed. It is known that RME can result in a phase undulation in azimuth direction [12], [13], which can be seen in the upper-left of Fig. 12(a). In this case, we estimated the RME by iteratively implementing the multisquint technique as shown in Fig. 13. We can see that the RME has reduced from 1.2 cm to $<$0.8 mm after four iterations. From Fig. 12(b), it is clear that the phase undulation has been successfully removed with the RME correction.

Hitherto, dual-antenna single-pass interferometry was used to correct the DEM error, and RME was also estimated and removed to acquire more reliable ground deformation. The results above demonstrated the feasibility of using BP algorithm to focus SAR data without traditional MoCo procedure. The major shortcoming of this BP algorithm is the heavy computational burden. However, thanks to the progress in computing technology, it can be easily mitigated by using alternate computing devices, such as graphics processing unit (GPU). For example, in this study, a desktop with a 1.8-GHz Quad Core CPU processor and two GeForce GTX TITAN X GPU devices were used to perform the BP focusing. For a SAR SLC image containing 4228 $\times$ 4404 pixels, the average processing time for BP focusing was 73 s. Therefore, the computational burden of the BP method was not a significant concern in this study.

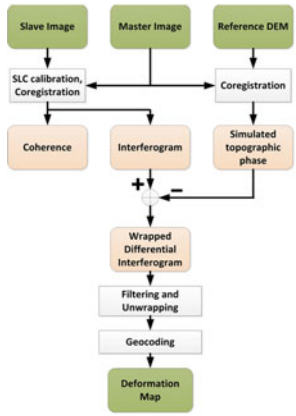

Fig. 14. Flowchart for spaceborne DInSAR processing.

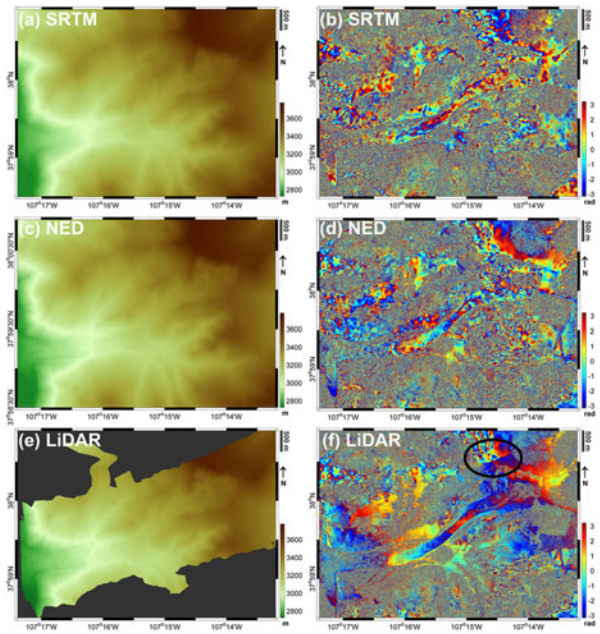

Fig. 15. Comparison of (a) SRTM, (c) NED, and (e) LiDAR DEMs along with the corresponding wrapped and geocoded spaceborne CSK differential interferograms in (b), (d), and (f), respectively. The spatial resolutions of SRTM, NED, and LiDAR DEMs are 30, 10, and 0.5 m, respectively. The CSK data pair 20150724–20150725 with a perpendicular baseline of -752 m was used to generate the interferograms. Circle in (f) denotes boundary of LiDAR DEM.

C. *Spaceborne DInSAR Processing*

A flowchart for traditional spaceborne DInSAR processing is shown in Fig. 14. Once we obtain an interferogram (and a coherence map) from the coregistered master and slave SLC images, the topographic phase contribution is removed using a reference DEM to generate a differential interferogram. Finally, a deformation map can be generated after filtering and unwrapping the differential interferogram.

In this study, we have tested SRTM DEM (30 m), National Elevation Dataset (NED) DEM (10 m), and LiDAR DEM (0.5 m) in CSK DInSAR processing as shown in Fig. 15. The

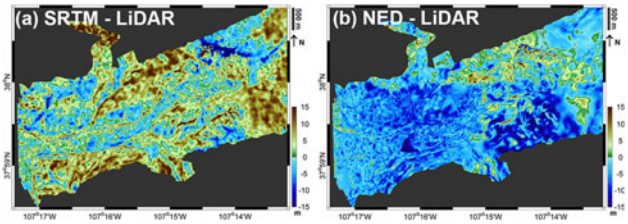

Fig. 16. Differences between SRTM and NED DEMs with the LiDAR DEM.

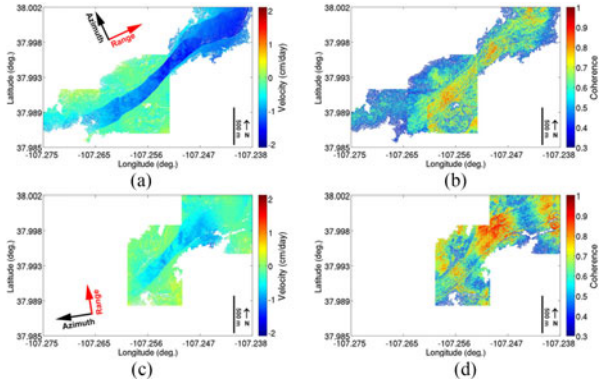

Fig. 17. Deformation maps and coherences from (a), (b) cross and (c), (d) parallel paths of the *L*-band airborne data acquisition. Areas with coherence less than 0.3 were discarded.

differential interferograms using both the SRTM and NED DEMs contain residual topographic phases over the landslide area [see Fig. 15(b) and (d)]. The residual phases are caused by the errors in the SRTM and NED DEMs, which was further confirmed by differencing the SRTM or NED DEMs with LiDAR DEM (see Fig. 16). On the other hand, Fig. 15(f) shows that the CSK DInSAR using the LiDAR DEM led to a better result (i.e., less residual phases). Note that the NED DEM was used for the area with no LiDAR coverage, and the black circle in Fig. 15(f) shows the boundary between NED and LiDAR DEMs. It is easy to see that the LiDAR DEM generated more reliable (smooth) results, whereas NED DEM caused residual phase errors. Even though SRTM and NED DEMs have already been successfully used in spaceborne DInSAR applications, the LiDAR DEM was needed in this study due to the changing topography of the landslide site as well as long spatial baselines as summarized in Table III. Therefore, LiDAR DEM was used for spaceborne CSK DInSAR processing to generate deformation maps.

IV. DInSAR Results

A. Airborne DInSAR Results

The estimated landslide velocities and the corresponding coherence maps from the airborne *L*-band DInSAR observations are shown in Fig. 17 [(a) and (b) from the paths across the landslide, and (c) and (d) from the parallel paths]. The areas with coherence lower than 0.3 were discarded. The coherences shown in Fig. 17(b) and (d) are relatively high (>0.6). The cross-path results [see Fig. 17(a)] show significant motion along the landslide (>1 cm/day). The neck area of the landslide shows the fastest motion, which is consistent with previous studies [25]–[31]. On the other hand, the parallel-path result [see Fig. 17 (c)] shows much slower landslide speeds (<1 cm/day). This is because the parallel-path's LOS direction is nearly perpendicular to the landslide flow direction, while the cross-path's LOS direction is almost parallel to the landslide flow direction.

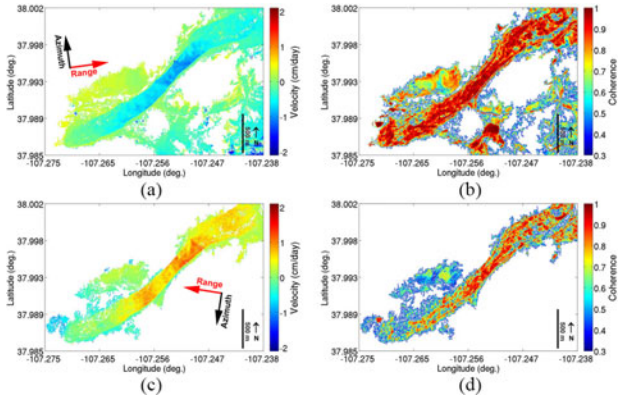

Fig. 18. Deformation maps and coherences from (a), (b) ascending and (c), (d) descending tracks of CSK spotlight scanning. Areas with coherence less than 0.3 were discarded.

B. Spaceborne DInSAR Results

Fig. 18 shows the landslide velocities obtained from the pairs of CSK data with the LiDAR DEM, and their corresponding coherences. In the ascending track geometry, the landslide moves toward the platform resulting in negative velocity values in Fig. 18(a). Using the descending pair, shown in Fig. 18(c), the landslide moves away from the satellite, which led to positive velocity values. From both the ascending and descending pairs, the maximum velocities were again observed around the "neck" of the landslide area. The coherences shown in Fig. 18(b) and (d) are high (>0.8) over most of the landslide area. However, over the nonlandslide area, the coherence is generally low (<0.5), which is caused by volume decorrelation due to vegetation [52] given that the CSK SAR system tends to be relatively sensitive because of its short *X*-band wavelength. Furthermore, as shown in Table III, the spatial baselines of the two interferometric pairs are relatively long (>750 m), which can exacerbate baseline decorrelation [52]. Due to the fast landslide motion, the vegetation on the landslide area is generally very sparse, leading to relatively higher coherence over the landslide.

By comparing Figs. 18 and 17, we can see that spaceborne DInSAR achieved higher coherence over the earthflow area. This may be due to the fact that the airborne SAR scannings were affected by aircraft turbulence while the orbits of the spaceborne platform were more stable. On the other hand, the airborne DInSAR results showed slightly better coherence around the forest areas outside the landslide than the CSK results. This could be due to CSK's shorter wavelength (*X*-band) and longer spatial baselines (>750 m). For the *L*-band airborne SAR, a pilot guidance system called "DragonFly" from Artemis, Inc., was used during the flight to ensure that the pilot flew the aircraft nearly the same track as the baseline flight [51]. Therefore, it was possible to maintain short spatial baselines (<15 m), which

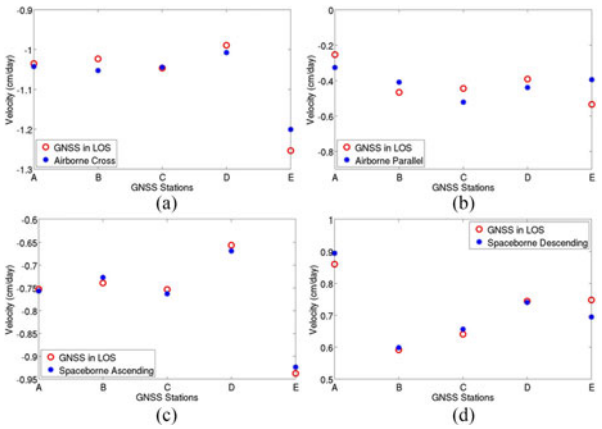

Fig. 19. Comparison of the GNSS-derived velocities in LOS directions with (a), (b) airborne, and (c), (d) spaceborne DInSAR results.

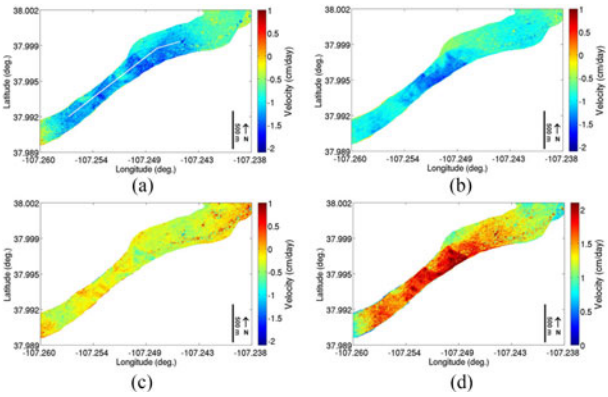

Fig. 20. Maps of the 3-D deformation components (a: North, b: East, and c: Vertical directions) estimated from two airborne and two spaceborne DInSAR LOS deformations. The absolute speed is shown in (d). The white line in (a) is a profile along the slide center which will be examined for further analysis.

allowed the airborne DInSAR system to have less baseline decorrelation.

V. Discussion

A. Comparison of GNSS and DInSAR Results in LOS Direction

In this section, the landslide motion estimates from airborne and spaceborne DInSAR are compared with deformation estimated by the five GNSS stations (see Fig. 1). The motion estimated from GNSS is considered to be the "true" 3-D deformation of the landslide while the DInSAR-derived deformation is motion projected onto the LOS direction. Therefore, in order to directly compare GNSS and DInSAR results, it is necessary to project the GNSS results onto the LOS direction. In this case, we projected the GNSS results onto four different LOS directions (corresponding to the LOS directions of the airborne cross and airborne parallel paths, as well as the spaceborne ascending, and spaceborne descending paths).

From the comparisons in Fig. 19, all of the airborne and spaceborne DInSAR results fit the GNSS results very well. The root mean square differences (RMSD) between the GNSS, and airborne and spaceborne DInSAR-derived velocities, are 0.6 and 0.2 mm/day, respectively. As stated earlier, the GNSS survey and the airborne SAR scanning were conducted between July 3 and July 10 of 2015, whereas the spaceborne CSK images were acquired between July 24 and July 26 of 2015. We can see from Fig. 19 that the spaceborne DInSAR estimation is still consistent with the GNSS results, and the deformation rate remained similar during the time period between July 10 and July 24 of 2015. This consistency enables us to generate a 3-D deformation map by combining the airborne and spaceborne DInSAR LOS deformation estimates, as presented in the following section.

B. 3-D Deformation Map

Given that the airborne and spaceborne DInSAR results agree with the GNSS results very well, it is possible to estimate 3-D motion of the landslide by combining their four different scanning geometries. First, we generated four deformation maps using both airborne and spaceborne CSK SAR datasets, as shown in Figs. 17 and 18, respectively. Then the LOS vectors were estimated using the trajectory (or orbit) information as well as the scanning geometry. Finally, for every pixel, the 3-D deformation vector was acquired using a least-squares inversion [55], [56]. The final 3-D deformation component maps are shown in Fig. 20 for the North, East, and Vertical directions. Fig. 20(a), (b), and most areas of (c) show that the landslide velocities have negative values in the North, East, and Vertical directions, which is consistent with the fact that the landslide moves in the South-West-Down direction. The upper right corner of Fig. 20(c) shows slightly positive values, which are caused by low coherence of the spaceborne DInSAR results in that area. Moreover, compared with the horizontal motion, the deformation in the vertical direction is much smaller ($<$0.5 cm/day). The absolute speed of the landslide motion is shown in Fig. 20(d), from which we can see that the "neck" of the landslide has the fastest speed of $\sim$2.1 cm/day. Similar deformation pattern has also been obtained from the UAVSAR measurements as shown in [36]. Due to different acquisition dates, our absolute deformation values are different from the UAVSAR results in [36]. Compared with UAVSAR system, one major advantage of SlimSAR system is its low cost. As a commercial product, the current market price of SlimSAR system is around $4 83 000. One way to compare the cost of SlimSAR and UAVSAR is to compare the usage fee. The current cost for UAVSAR G3 flight hours is approximately $2500 per flight hour [42] while it costs about $500 to $1000 per flight hour for SlimSAR.

As shown in Fig. 21, the RMS errors (RMSEs) from the least-squares inversion of the estimated 3-D deformation in the North, East, and Vertical directions were generally small ($<$ 0.2 cm/day) over most of the landslide area. The upper right part of the landslide shows slightly larger error, which is again caused by low coherence, especially for the airborne SAR parallel flight as shown in Fig. 17(d) and the CSK DInSAR results as shown in Fig. 18.

In order to further visualize the motion pattern of the landslide, the horizontal deformation is illustrated with color-coded arrows in Fig. 22(a). It is easy to see that the direction of the

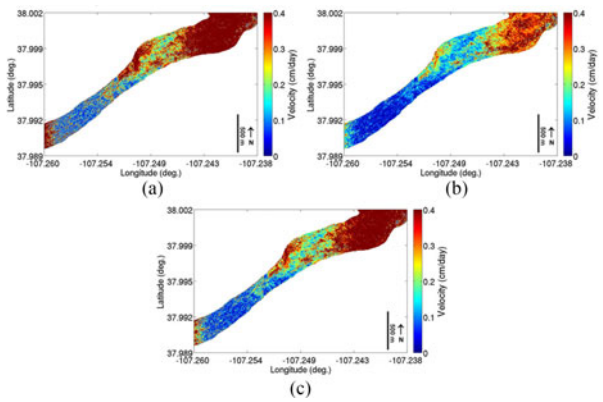

Fig. 21. Least-squares inversion RMSEs of the estimated 3-D deformation components in the North, East, and Vertical directions. (a) North. (b) East. (c) Vertical.

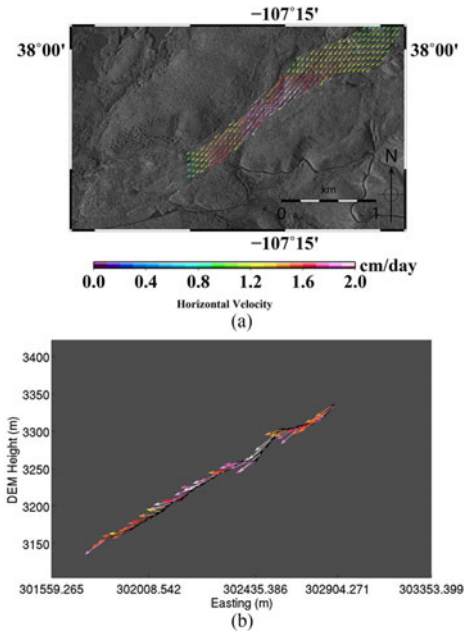

Fig. 22. (a) Downsampled horizontal velocity field, and (b) vertical velocity field of a profile along the center profile of the landslide shown in Fig. 20(a). The background in (a) is the spaceborne SAR amplitude image. The x-axis in (b) is the easting coordinates given in Universal Transverse Mercator coordinate system in meters.

landslide motion is along the "flow" direction of the earthflow and the "neck" area has the fastest motion. A profile of 3-D deformation along the center line shown in Fig. 20(a) is plotted with arrows in Fig. 22(b). The topography from the airborne LiDAR DEM is used to generate the elevation profile. As would be expected, we find that the direction of the landslide is highly related to the variation of the topography, especially over the upper part of the landslide. When the slope of the topography becomes steeper, the landslide speed increases and the motion direction changes with changes in the topographic slope.

C. Comparison of GNSS and DInSAR-Derived 3-D Deformation Map

After generating the 3-D deformation map it is necessary to compare the 3-D velocities derived from the spaceborne and airborne combined observations with the velocities obtained from the GNSS observations. The results of this comparison are shown in Fig. 23 and show overall good agreement between them. The RMSDs between the GNSS and DInSAR-derived velocities in North, East, and Vertical directions were 1.2, 0.2, and 0.4 mm/day, respectively. The comparison in the North direction shows a slightly larger difference, which could be due to the fact that spaceborne DInSAR is less sensitive to the deformation in the North–South direction.

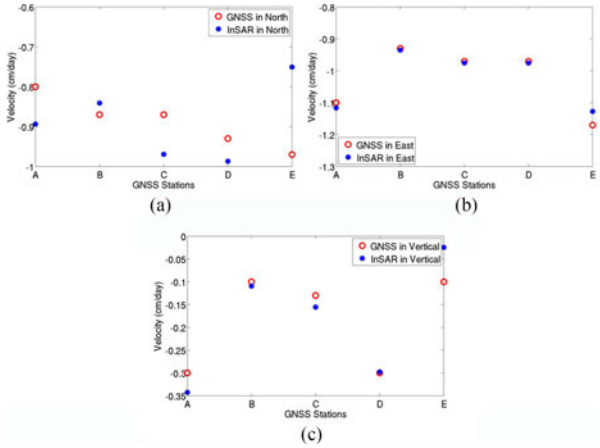

Fig. 23. Comparison of GNSS and DInSAR-derived 3-D deformation map in North, East, and Vertical directions.

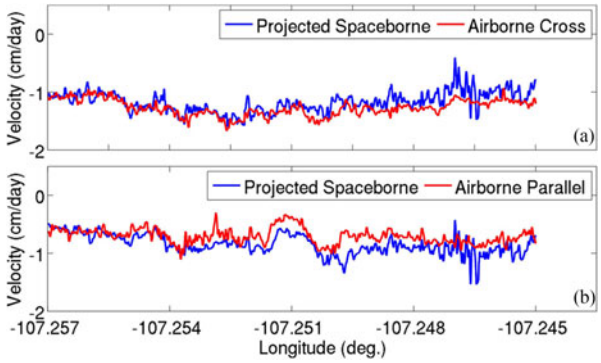

Fig. 24. Comparison of the airborne and spaceborne DInSAR results along the center of the landslide. (a) and (b) shows the spaceborne results projected on the LOS directions of the airborne cross and parallel tracks, respectively.

D. Comparison of Airborne and Spaceborne DInSAR Results

The previous sections analyzed the 3-D deformation estimated from the four airborne and spaceborne LOS deformations. It was already shown that both the airborne and spaceborne DInSAR fit the GNSS results very well. In this section, we attempt to directly evaluate the performance of the airborne DInSAR using the spaceborne DInSAR results. It should be noted that it is not possible to directly compare them because they were acquired with different LOS directions. However, as discussed in Section V-B, the motion direction is correlated with the surface gradient. Assuming motion is along the surface gradient, a "3-D deformation" can be generated using spaceborne measurements only. Then we projected the "3-D deformation" to the LOS directions of the airborne cross and parallel

flights, respectively. Finally, we directly compared the projected spaceborne results with the airborne results as shown in Fig. 24. We can see that the airborne DInSAR results show similar spatial patterns and agree well with the spaceborne DInSAR results. The values of the R^2 parameters and RMSD are 0.47 and 1 mm/day for airborne cross track, and 0.34 and 1.1 mm/day for airborne parallel track, respectively. The deviations in Fig. 24 could be caused by the errors of the estimated gradient directions, or the bias between the surface gradient directions and the real-motion directions.

VI. Conclusion

In this paper, airborne DInSAR observations of the Slumgullion landslide, processed using the time-domain BP algorithm, were presented. Dual-antenna single-pass interferometry was performed to remove the SRTM DEM error through the iterative process and RME was also corrected using the multisquint method. The airborne DInSAR results showed good agreement with those of GNSS and spaceborne DInSAR results. The RMSD between the airborne DInSAR and GNSS results was 0.6 mm/day. A 3-D deformation map was also generated by integrating the airborne and spaceborne DInSAR results from four different LOS directions. The map showed that the maximum landslide speed was $\sim$2.1 cm/day, and there exists a relationship between the landslide motion and topographic variation. We demonstrated that the airborne DInSAR system using the BP algorithm has a potential to provide time-transient variability in land surface topography with high precision (centimetric with *L*-band) and high resolution ($<$1 m). The successful application of airborne DInSAR using BP could open new avenues for scientific studies and commercial applications with greater flexibility in selecting the temporal and spatial baselines of the datasets.

Acknowledgment

The authors would like to thanks the NCALM staff and graduate students for conducting the airborne LiDAR and in-situ GNSS campaigns, in particular, X. Zhu for processing the differential GNSS data. The authors would also like to thank the anonymous reviewers for their valuable suggestions and comments.

References

[1] Y. Morishita, T. Kobayashi, and H. Yarai, "Three-dimensional deformation mapping of a dike intrusion event in Sakurajima in 2015 by exploiting the rightand left-looking ALOS-2 InSAR," *Geophys. Res. Lett.*, vol. 43, pp. 4197–4204, May 2016.

[2] E. Zaugg, M. Edwards, and A. Margulis "The SlimSAR: A small, multifrequency, synthetic aperture radar for UAS operation," in *Proc. IEEE Radar Conf.*, May 10–14, 2010, pp. 277–282.

[3] A. Reigber and R. Scheiber, "Airborne differential SAR interferometry: First results at L-band," *IEEE Trans. Geosci. Remote Sens.*, vol. 41, no. 6, pp. 1516–1520, Jun. 2003.

[4] S. Hensley, H. Zebker, C. Jones, T. Michel, R. Muellerschoen, and B. Chapman, "First deformation results using the NASA/JPL UAVSAR instrument," in *Proc. 2nd Asian-Pac. Conf. Synthetic Aperture Radar*, Oct. 2009, pp. 1051–1055.

[5] S. Perna, C. Wimmer, J. Moreira, and G. Fornaro, "X-band airborne differential interferometry: Results of the OrbiSAR campaign over the Perugia area," *IEEE Trans. Geosci. Remote Sens.*, vol. 46, no. 2, pp. 489–503, Feb. 2008.

[6] A. Moreira and Y. Huang, "Airborne SAR processing of highly squinted data using a chirp scaling approach with integrated motion compensation," *IEEE Trans. Geosci. Remote Sens.*, vol. 32, no. 5, pp. 1029–1040, Sep. 1994.

[7] G. Fornaro, "Trajectory deviations in airborne SAR: Analysis and compensation," *IEEE Trans. Aerosp. Electron. Syst.*, vol. 35, no. 3, pp. 997–1009, Jul. 1999.

[8] P. Prats, A. Reigber, and J. J. Mallorqui, "Topography-dependent motion compensation for repeat-pass interferometric SAR systems," *IEEE Geosci. Remote Sens. Lett.*, vol. 2, no. 2, pp. 206–210, Apr. 2005.

[9] K. A. C. de Macedo and R. Scheiber, "Precise topography- and aperture-dependent motion compensation for airborne SAR," *IEEE Geosci. Remote Sens. Lett.*, vol. 2, no. 2, pp. 172–176, Apr. 2005.

[10] G. Fornaro, G. Franceschetti, and S. Perna, "Motion compensation errors: Effects on the accuracy of airborne SAR images," *IEEE Trans. Aerosp. Electron. Syst.*, vol. 41, no. 4, pp. 1338–1352, Oct. 2005.

[11] P. Prats, K. A. C. de Macedo, A. Reigber, R. Scheiber, and J. J. Mallorqui, "Comparison of topography-dependent motion compensation algorithms for airborne SAR," *IEEE Geosci. Remote Sens. Lett.*, vol. 4, no. 3, pp. 349–353, Jul. 2007.

[12] A. Reigber, "Correction of residual motion errors in airborne SAR interferometry," *Electron. Lett.*, vol. 37, no. 17, pp. 1083–1084, Aug. 2001.

[13] P. Prats and J. J. Mallorqui, "Estimation of azimuth phase undulations with multisquint processing in airborne interferometric SAR images," *IEEE Trans. Geosci. Remote Sens.*, vol. 41, no. 6, pp. 1530–1533, Jun. 2003.

[14] A. Reigber, P. Prats, and J. J. Mallorqui, "Refined estimation of time-varying baseline errors in airborne SAR interferometry," *IEEE Trans. Geosci. Remote Sens.*, vol. 3, no. 1, pp. 145–149, Jan. 2006.

[15] A. Reigber *et al.*, "Very-high-resolution airborne synthetic aperture radar imaging: Signal processing and applications," *Proc. IEEE*, vol. 101, no. 3, pp. 784–797, Mar. 2013.

[16] S. Hensley *et al.*, "Residual motion estimation for UAVSAR: Implications of an electronically scanned array," in *Proc. Radar Conf.*, Pasadena, CA, USA, May 2009, pp. 1–5.

[17] K. A. C. Macedo, R. Scheiber, and A. Moreira, "An autofocus approach for residual motion errors with application to airborne repeat-pass SAR interferometry," *IEEE Trans. Geosci. Remote Sens.*, vol. 46, no. 10, pp. 3151–3162, Oct. 2008.

[18] G. Fornaro, G. Franceschetti, and S. Perna, "On center-beam approximation in SAR motion compensation," *IEEE Trans. Geosci. Remote Sens.*, vol. 3, no. 2, pp. 276–280, Apr. 2006.

[19] M. Soumekh, *Synthetic Aperture Radar Signal Processing: With MATLAB Algorithms*. Hoboken, NJ, USA: Wiley, 1999.

[20] J. C. Curlander and R. N. McDonough, *Synthetic Aperture Radar—Systems and Signal Processing*. Hoboken, NJ, USA: Wiley, 1991.

[21] A. F. Yegulalp, "Fast backprojection algorithm for synthetic aperture radar," in *Proc. Rec. IEEE Radar Conf.*, 1999, pp. 60–65.

[22] L. M. H. Ulander, H. Hellsten, and G. Stenström, "Synthetic-aperture radar processing using fast factorized back-projection," *IEEE Trans. Aerosp. Electron. Syst.*, vol. 39, no. 3, pp. 760–776, Jul. 2003.

[23] O. Frey, C. Magnard, M. Rüegg, and E. Meier, "Focusing of airborne synthetic aperture radar data from highly nonlinear flight tracks," *IEEE Trans. Geosci. Remote Sens.*, vol. 47, no. 6, pp. 1844–1858, Jun. 2009.

[24] M. I. Duersch and D. G. Long, "Analysis of time-domain backprojection for stripmap SAR," *Int. J. Remote Sens.*, vol. 36, no. 8, pp. 2010–2036, Apr. 2015, doi: 10.1080/01431161.2015.1030044.

[25] M. Parise and R. Guzzi, "Volume and shape of the active and inactive parts of the Slumgullion landslide, Hinsdale County, Colorado," U.S. Geological Survey, Reston, VA, USA, Open—File Report 92-216, 1992, p. 29.

[26] D. J. Varnes and W. Z. Savage, "The Slumgullion earth flow: A large-scale natural laboratory," U.S. Geological Survey, Reston, VA, USA, Bulletin 2130, 1996, p. 95.

[27] R. W. Fleming, R. L. Baum, and M. Giardino, "Map and Description of the active part of the Slumgullion landslide, Hinsdale County, Colorado. U.S.,' Geological Survey Geologic Investigations Series Map I-2672, 1999, p. 34.

[28] J. Coe *et al.*, "Seasonal movement of the Slumgullion landslide determined from global positioning system surveys and field instrumentation, July 1998–March 2002," *Eng. Geol.*, vol. 68, pp. 67–101, 2003.

[29] W. H. Schulz, J. P. McKenna, G. Biavati, and J. D. Kibler, "Relations between hydrology and velocity of a continuously moving landslide—Evidence of pore-pressure feedback regulating landslide motion?" *Landslides*, vol. 6, pp. 181–190, 2009.

[30] W. H. Schulz *et al.*, "Kinematics of the Slumgullion landslide revealed by ground-based InSAR surveys," in *Proc. 11th Int. 2nd North Amer. Symp. Landslides Engineered Slopes*, Banff, AB, Canada, Jun. 3–8, 2012, pp. 1273–1279.
[31] J. S. Gomberg, W. H. Schulz, P. Bodin, and J. W. Kean, "Seismic and geodetic signatures of fault slip at the Slumgullion landslide natural laboratory," *J. Geophys. Res.*, vol. 116, 2011, Art. no. B09404, doi: 10.1029/2011JB008304.
[32] E. C. Zaugg, J. P. Bradley, H. Lee, and N. Cao. "Differential interferometric SAR At multiple frequencies over the slumgullion earthflow," in *Proc. IEEE Radar Conf.*, May 2–6, 2016, pp. 1–6.
[33] B. Delbridge, R. Burgmann, E. Fielding, and S. Hensley, "Kinematics of the slumgullion landslide from UAVSAR derived interferograms," in *Proc. Int. Geosci. Remote Sens. Symp.*, Milan, Italy, Jul. 26–31, 2015, pp. 3842–3845.
[34] P. Milillo, E. J. Fielding, W. H. Shulz, B. Delbridge, and R. Burgmann, "COSMO-SkyMed spotlight interferometry over rural areas: The slumgullion landslide in colorado, USA," *IEEE J. Sel. Topics Appl. Earth Observ. Remote Sens.*, vol. 7, no. 7, pp. 2919–2926, Jul. 2014.
[35] B. G. Delbridge, R. Burgmann, E. J. Fielding, S. Hensley, and W. H. Schulz, "Surface flow kinematics derived from airborne UAVSAR interferometric synthetic aperture radar to constrain the physical mechanisms controlling landslide motion," in *Proc. Amer. Geophys. Union Fall Meeting*, 2013, vol. 1, Paper 2013-G33D-08.
[36] B. G. Delbridge, R. Burgmann, E. J. Fielding, S. Hensley, and W. H. Schulz, "Three-dimensional surface deformation derived from airborne interferometric UAVSAR: Application to the Slumgullion landslide," *J. Geophys. Res. Solid Earth*, vol. 121, pp. 3951–3977, 2016.
[37] Z. Lu, J. Zhang, Y. Zhang, and D. Dzurisin, "Monitoring and characterizing natural hazards with satellite InSAR imagery," *Ann. GIS*, vol. 16, pp. 55–66, 2010.
[38] R. Horn, "The DLR airborne SAR project E-SAR," in *Proc. IEEE Int. Geosci. Remote Sens. Symp.*, 1996, vol. 3, pp. 1624–1628.
[39] R. Horn, A. Nottensteiner, and R. Scheiber, "F-SAR-DLR's advanced airborne SAR system onboard DO228," in *Proc. 7th Eur. Conf. Synthetic Aperture Radar*, Friedrichshafen, Germany, Jun. 2008, vol. 4, pp. 195–198.
[40] Y. Lou *et al.*, "UAVSAR Instrument: Current operations and planned upgrades," ESTF 2011 (Earth Science Technology Forum 2011), Pasadena, CA, USA, Jun. 21–23, 2011.
[41] K. A. C. de Macedo *et al.*, "Long-term airborne DInSAR measurements at X- and P-bands: A case study on the application of surveying Geohazard threats to pipelines," *IEEE J. Sel. Topics Appl. Earth Observ. Remote Sens.*, vol. 5, no. 3, pp. 990–1005, Jun. 2012.
[42] Jul. 2017. [Online]. Available: https://uavsar.jpl.nasa.gov/help/faq.html.
[43] G. Wang, "GPS landslide monitoring: Single base vs. network solutions: A case study based on the Puerto Rico and Virgin Islands permanent GPS network," *J. Geodetic Sci.*, vol. 1, pp. 191–203, Apr. 2011.
[44] G. Wang, "Kinematics of the Cerca del Cielo, Puerto Rico landslide derived from GPS observations," *Landslides*, vol. 9, pp. 117–130, May 2011.
[45] R. Bürgmann, P. A. Rosen, and E. J. Fielding, "Synthetic aperture radar interferometry to measure Earth's surface topography and its deformation," *Ann. Rev. Earth Planet. Sci.*, vol. 28, pp. 169–209, 2000.
[46] D. Massonnet and K. Feigl, "Radar interferometry and its application to changes in the Earth's surface," *Rev. Geophys.*, vol. 36, pp. 441–500, 1998.
[47] P. A. Rosen *et al.*, "Synthetic aperture radar interferometry," *Proc. IEEE*, vol. 88, no. 3, pp. 333–380, Mar. 2000.
[48] May 2016. [Online]. Available: https://www.novatel.com/assets/Documents/Papers/FSAS.pdf
[49] Feb. 2010. [Online]. Available: https://ti.arc.nasa.gov/dataset/KrexDataBasaltHills2012/refdoc/HG1700_SPAN.pdf
[50] *COSMO-SkyMed SAR Products Handbook*. Rome, Italy: ASI, Agenzia Spaziale Italiana, 2007.
[51] E. Zaugg and M. Edwards, "Experimental results of repeat-pass SAR employing a visual pilot guidance system," in *Proc. IEEE Radar Conf.*, Atlanta, GA, USA, May 7–11, 2012, pp. 629–634.
[52] H. A. Zebker and J. Villasenor, "Decorrelation in interferometric radar echoes," *IEEE Trans. Geosci. Remote Sens.*, vol. 30, no. 5, pp. 950–959, Sep. 1992.
[53] M. I. Duersch and D. G. Long, "Backprojection SAR interferometry," *Int. J. Remote Sens.*, vol. 36, no. 4, pp. 979–999, 2015.
[54] M. I. Duersch, "Backprojection for synthetic aperture radar," Ph.D. dissertation, Brigham Young Univ., Provo, UT, USA, 2013.
[55] T. J. Wright, B. E. Parsons, and Z. Lu, "Toward mapping surface deformation in three dimensions using InSAR," *Geophys. Res. Lett.*, vol. 31, no. 1, Jan. 2004, Art. no. L01607, doi:10.1029/2003GL018827.
[56] G. J. Funning, B. Parsons, T. J. Wright, J. A. Jackson, and E. J. Fielding, "Surface displacements and source parameters of the 2003 Bam (Iran) earthquake from envisat advanced synthetic aperture radar imagery," *J. Geophys. Res.*, vol. 110, no. B9, Sep. 2005. Art. no. B09406, doi:10.1029/2004JB003338.

Ning Cao received the B.S. and M.S. degrees in electronic engineering from Harbin Institute of Technology, Harbin, China, in 2011 and 2013, respectively, and the Ph.D. degree in geosensing systems engineering and sciences from the Department of Civil and Environmental Engineering, University of Houston, Houston, TX, USA, in 2016.

He is currently a Postdoc in the Department of Civil and Environmental Engineering and the National Center for Airborne Laser Mapping, University of Houston, Houston, TX, USA. His main research interests include multitemporal interferometric SAR techniques, airborne SAR/InSAR.

Hyongki Lee received the B.S. and M.S. degrees in civil engineering from Yonsei University, Seoul, South Korea, in 2000 and 2002, respectively, and the Ph.D. degree in geodetic science from Ohio State University, Columbus, OH, USA, in 2008.

He is currently an Associate Professor in the Department of Civil and Environmental Engineering and the National Center for Airborne Laser Mapping, University of Houston, Houston, TX, USA.

Dr. Lee received the NASA New Investigator Award in Earth Science.

Evan Zaugg received the B.S. and Ph.D. degrees in electrical engineering from Brigham Young University, Provo, UT, USA, in 2005 and 2010, respectively.

At ARTEMIS, Inc., he continues his research and development of SAR systems, data processing, and exploitation, including advanced SAR image formation algorithms, ground moving target indicators, interferometry, and change detection.

Ramesh Shrestha, photograph and biography not available at the time of publication.

William Carter, photograph and biography not available at the time of publication.

Craig Glennie, photograph and biography not available at the time of publication.

Guoquan Wang, photograph and biography not available at the time of publication.

Zhong Lu, photograph and biography not available at the time of publication.

Juan Carlos Fernandez-Diaz, photograph and biography not available at the time of publication.